43rd AIAA Aerospace Sciences Meeting
January 10–13, 2005
Reno, NV

AIAA 2005-1223

Characterization of Space Shuttle Ascent Debris Aerodynamics Using CFD Methods

Scott M. Murman*
ELORET Corp.
MS T27B
Moffett Field, CA 94035

Michael J. Aftosmis† and Stuart E. Rogers‡
NASA Ames Research Center
MS T27B
Moffett Field, CA 94035

Abstract

An automated Computational Fluid Dynamics process for determining the aerodynamic characteristics of debris shedding from the Space Shuttle Launch Vehicle during ascent is presented. This process uses Cartesian fully-coupled, six-degree-of-freedom simulations of isolated debris pieces in a Monte Carlo fashion to produce models for the drag and crossrange behavior over a range of debris shapes and shedding scenarios. A validation of the Cartesian methods against ballistic range data for insulating foam debris shapes at flight conditions, as well as validation of the resulting models, are both contained. These models are integrated with the existing shuttle debris transport analysis software to provide an accurate and efficient engineering tool for analyzing debris sources and their potential for damage.

1 Introduction

Video analysis of the ascent of space shuttle mission STS-107 in January 2003 showed that an object shed from the bipod-ramp region impacted the left wing of the orbiter[1]. Subsequently, NASA and the Columbia Accident Investigation Board (CAIB) initiated a transport

*Senior Research Scientist, smurman@mail.arc.nasa.gov, Member AIAA
†Aerospace Engineer, maftosmis@mail.arc.nasa.gov, Senior Member AIAA
‡Aerospace Engineer, serogers@mail.arc.nasa.gov, Associate Fellow AIAA

analysis of this event to determine a credible flight path and impact velocity for the piece of debris. This debris transport analysis was performed both during the mission, and after the subsequent accident upon re-entry. The analysis provided an accurate prediction of the velocity a large piece of the left foam bipod ramp would have as it impacted the wing leading edge (*cf.* [1], *pg.* 61). This prediction was corroborated by both the video analysis and fully-coupled CFD/6-DOF simulations[2]. While the prediction of impact velocity was sufficiently accurate to predict critical damage in this case, one of the recommendations of the CAIB for Return-To-Flight (RTF) was to analyze the complete debris environment experienced by the Space Shuttle Launch Vehicle (SSLV) on ascent. This analysis includes categorizing all possible debris sources, their probable geometric and aerodynamic characteristics, and their potential for damage.

This paper is chiefly concerned with predicting the aerodynamic characteristics of a variety of potential debris sources (insulating foam, ice, ...) for the SSLV using Computational Fluid Dynamics (CFD) methods. These aerodynamic characteristics are used in the debris transport analysis to predict flight path, impact velocity and angle, and provide a statistical distribution to support risk analyses where appropriate. A ballistic code predicts the velocity of debris which potentially impact the SSLV during ascent using a drag model tailored for each separate debris source. Similarly, a method of accounting for the aerodynamic lift is required in order to determine the potential debris impact locations. These lift and drag aerodynamic models are supplied by the automated CFD process described here.

The aerodynamic characteristics of debris are difficult to determine using traditional methods, such as static or dynamic test data. The debris trajectories are highly non-linear, involving uncontrolled three-axis rotations. Hence, traditional aerodynamic modeling techniques developed for controlled maneuvers of aerodynamically-trim aircraft are not sufficient. Free-flight ballistic range testing can provide trajectory data to use in model development, however, this type of testing is time-consuming, costly, and limited in the types of shapes and conditions that can be efficiently tested. Unsteady 6-DOF CFD methods provide the same trajectory data as free-flight testing without these limitations: CFD methods can efficiently provide hundreds of trajectories overnight for an arbitrary geometry. The use of numerical simulations frees the ballistic testing to concentrate on a critical subset of the requirements, such as structural limit testing or reference validation cases.

The current work describes NASA's use of a Cartesian mesh, moving-boundary solver coupled with a 6-DOF module[3, 4] to efficiently provide the data for developing the drag and crossrange models. The Cartesian package can automatically handle arbitrary geometric shapes, and perform steady-state, prescribed-motion, or fully-coupled 6-DOF simulations using an efficient parallel, multi-level infrastructure. This package provides the analyst with a push-button tool for simulating static wind tunnel, rotary-balance, or ballistic range tests computationally. This ability complements and extends the traditional physical test facilities, providing a cost-effective approach for aerodynamic modeling of complex dynamic events.

The current paper describes and demonstrates a process for using automated 6-DOF CFD methods to develop aerodynamic models for shuttle ascent debris. The first section provides background information on the debris transport analysis, including details of the tools and a computed 6-DOF validation against reference ballistic range data. The next

section analyzes in detail the aerodynamic modeling of insulating foam debris shed from the shuttle external tank (ET). The details of the modeling process are presented, along with validation of both the methods used, and the models developed, for foam debris. Lastly, the main topics of the paper are summarized.

2 Background

Ascent debris has been a constant threat throughout the history of launch vehicle development. As sketched in Figure 1, the analysis of the shuttle ascent debris environment is an iterative process. The debris sources and their aerodynamic characteristics are fed into the debris transport code, which calculates trajectory information to provide an assessment of the potential damage or risk from a particular debris source to a particular structural component (e.g. ET foam impacting the orbiter wing). This damage assessment is provided to the separate structural components of the shuttle, which then must determine whether they can safely withstand the damage. This structural analysis in turn is fed back into the process, as debris sources which cannot be safely tolerated are eliminated through design or manufacturing process modifications. In order for this iterative procedure to be effective, the debris transport analysis must be rapid. It is common for hundreds of thousands of trajectories to be analyzed over the entire vehicle at each iteration.

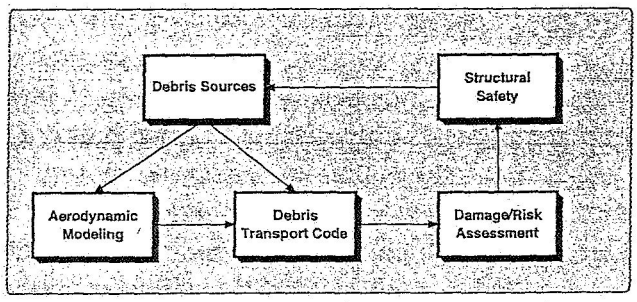

Figure 1: Debris analysis feedback loop. Damage from potential debris sources is assessed, and those which are not tolerable are eliminated. This cycle then continues until a safe tolerance is achieved.

To provide an efficient engineering tool, the debris transport analysis code simplifies several aspects of the problem. The first approximation is that the debris has no effect on the flowfield: the transport code queries the local flow conditions from a high-resolution, static, viscous flow simulation of the shuttle flowfield provided by the OVERFLOW solver[5] at the appropriate flight conditions for the debris event. A ballistic model is applied in the direction of the local flow velocity to determine the deceleration and "zero-lift" trajectory. The version of the debris transport code used in the STS-107 investigation applied an initial velocity to the debris in order to simulate the dispersion due to aerodynamic lift. The code does not directly account for any potential rotation of the body. With these approximations the debris transport code can analyze a single debris trajectory through the shuttle flowfield in a milliseconds of CPU time, while simulating a debris piece moving relative to the SSLV using a fully-coupled 6-DOF CFD method requires hundreds of CPU-hours. Without sacrificing this efficiency, it is desired to improve the accuracy of the debris transport code. These improvements include a realistic modeling of the dispersions about the zero-lift trajectory due to aerodynamic lift, and drag models tailored to the different debris sources. Both of these enhancements to the transport code require a detailed knowledge of the aerodynamics

of free-flying debris.

2.1 Numerical Scheme

Characterizing the aerodynamics of dynamic debris shedding events from the shuttle stack on ascent requires the ability to efficiently compute static, prescribed-motion, and coupled 6-DOF simulations. The implicit Cartesian moving-boundary solver described in [3] and [4] fulfills these requirements. The mesh generation is automated, and parameter studies of the various dynamic scenarios experienced by the debris are automatically handled by the Geometry Manipulation Protocol (GMP) interface [6]. Characterizing the debris trajectories often requires a Monte Carlo approach making automated methods a necessity. The aerodynamic characterization investigates an isolated piece of dynamic debris in a uniform stream, moving under the influence of aerodynamic forces. This results in a time-dependent coupling between the fluid dynamics and the motion of the body. This coupled CFD/6-DOF scenario is efficiently and accurately simulated using the Arbitrary Lagrangian-Eulerian (ALE) rigid-domain motion capability of the solver. The ALE scheme allows the motion of the debris to be handled entirely within the software of the flow solver without requiring complicated and costly inter-mesh communications between timesteps. Complete details on the numerical algorithms are presented in [3] and [4]. Validation for unconstrained, isolated debris pieces will be presented for representative shapes and flight conditions in the next sections.

Performing fully-coupled 6-DOF simulations of multiple debris sources at various flight conditions requires an automated process. This process is outlined schematically in Fig. 2. The green boxes represent inputs to the system (geometry, flight conditions, initial orientation and rates), the orange boxes represent steps within the CFD process (mesh generator, flow solver, ...), and the drag and crossrange data is obtained as an output. This system is completely automated, with scripts used to glue separate modules together. The following list provides a brief synopsis of each module in Fig. 2:

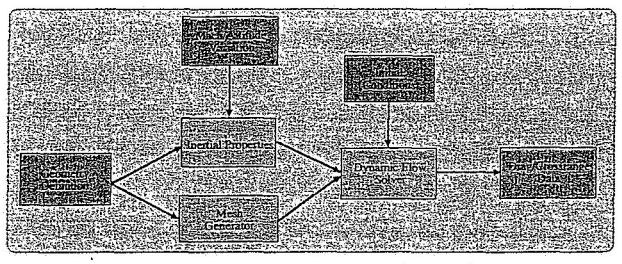

Figure 2: Process diagram for Monte Carlo 6-DOF trajectory analysis. Green boxes are process inputs which are given a range of inputs, orange boxes are internal modules, and the purple box is output fed to the debris transport software.

- The geometry is usually specified with a CAD solid model, either from an analytic definition or from 3-D digitized data. The CAD geometry is automatically triangulated and passed to the Cartesian mesh generator.
- A typical Cartesian mesh for an isolated debris piece will contain between 200-300k cells, and can be automatically generated in a matter of seconds of CPU time.
- The dynamics of the debris is dependent upon the altitude. Data for the shuttle ascent trajectory is available in pre-flight tables which are queried to obtain the correlation of altitude with vehicle Mach number.

- The inertial properties are calculated from the triangulated shape by assuming a uniform material density, which is specified as an input.
- The initial rotation orientation and rate must be specified for each 6-DOF simulation. These inputs should be consistent with the debris shedding mechanism. Examples will be given in the next section for foam debris.
- A single trajectory calculation requires 30-60 CPU-hours on the NASA Ames Altix system. This system has a total of 10240 CPUs which provides enough throughput to easily run hundreds of trajectories in a day using only a fraction of the computational resources.

Much of the aerodynamic modeling of debris requires a Monte Carlo approach to the 6-DOF trajectory calculations. In these cases the geometry is held fixed, and the flight conditions and initial orientation and rotation rate of the debris are varied, with multiple trajectories being run in parallel.

2.2 Dynamic Cube Validation

The Cartesian moving-body solver has been validated for a variety of aerodynamic problems, including store separation, dynamic missile configurations, and transonic flutter[3, 8, 9]. The requirements of simulating debris shedding from the shuttle on ascent are unique however, and further validation for these situations is required. Unfortunately there is a dearth of relevant dynamic data for objects being released at high Mach numbers and high altitude. Hansche and Rinehart[7] fired 1/4" and 3/8" steel cubes from a gun at sea-level and measured the drag through the supersonic Mach number range. This data is especially relevant for comparison as the ballistic drag model used in the debris transport code for the STS-107 investigation is based upon this data, i.e. all debris sources are assumed to be roughly shaped like cubes. Obviously this assumption does not hold for general shapes, and the purpose of this work is to develop a process which can efficiently generate appropriate drag models for specific debris shapes. Figure 3 presents the computed drag coefficient variation against the free-flight range data, using several different simulation methods. Static simulations were performed with the cube held fixed with the minimum and maximum frontal area exposed to the wind respectively. These computations trace the lower and upper bounds of the experimental scatter. In order to simulate an "average" dynamic motion, the cube was rotated at

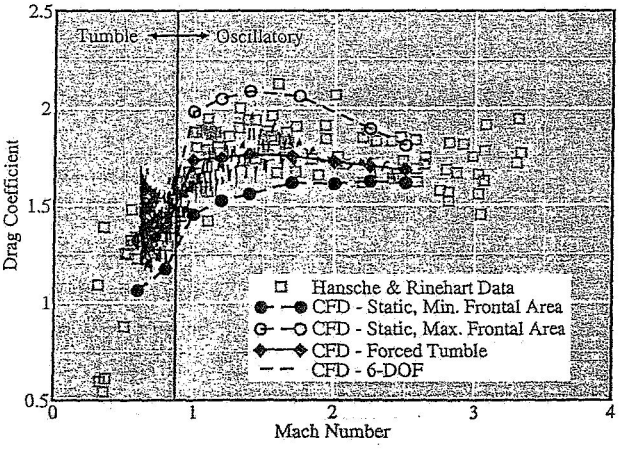

Figure 3: Drag coefficient variation for a cube. Static, forced-tumble, and 6-DOF simulations are compared against ballistic range data from [7].

a constant rate about all three axes at a fixed Mach number. The average of these dynamic simulations over a complete cycle is termed a "forced-tumble" simulation. The forced tumble results for the cube bisect the experimental scatter. The final type of simulation included in Fig. 3 is a 6-DOF simulation with the cube being released into a uniform stream and allowed to decelerate and rotate under the influence of the aerodynamic loads. This 6-DOF curve shows the cube begin to oscillate as the separation buffets the body, eventually leading to a tumbling motion as the cube passes through the transonic regime. The drag prediction from the 6-DOF trajectory also falls within the experimental data. The ensemble average of many 6-DOF trajectories released with different initial conditions (orientation, rotation rate) collapses to the forced-tumble prediction in this case.

Of note in the dynamic cube simulations is that the cube does not tumble immediately. The cube shape is statically-stable in a supersonic flow, which is a necessary, but not sufficient, condition to ensure dynamic stability. As the body rotates, the bow shock ahead of the body reacts, generating a restoring moment. Simulations in which the cube is given an initial rotation rate and then released exhibit the same behavior - an oscillation about the static stability point in supersonic flow, and a tumbling motion in the transonic regime as the dynamic pressure decreases sufficiently so that the restoring aerodynamic moment on the cube is not sufficient to maintain the stable oscillation. The rotational inertia of the cube under these conditions is not sufficient to overcome the static stability. This same type of dynamic behavior will be seen in the results for the conical foam divots in the next section.

3 Foam Debris

The CAIB determined that the likely cause of the STS-107 accident was a piece of insulating foam being shed from the bipod attachment region of the ET and impacting the Reinforced Carbon-Carbon (RCC) thermal protection system on the leading-edge of the orbiter wing. While this particular threat has been removed by a re-design of the bipod region, the CAIB also noted that the shuttle has a history of numerous debris shedding events, including strikes to the orbiter, emanating from the insulating foam covering the ET (cf. [1], pg. 127). The regions of the ET where insulating foam is applied are noted in Fig. 4. The physical similarity of the insulating foam on the ET to the cause of the STS-107 accident indicates that thoroughly analyzing these ET debris events is of primary importance for RTF. This section discusses the aerodynamic modeling of insulating foam debris from the ET, including validation of the numerical methods for these shapes and conditions, demonstration of the model development, validation of the model itself, and

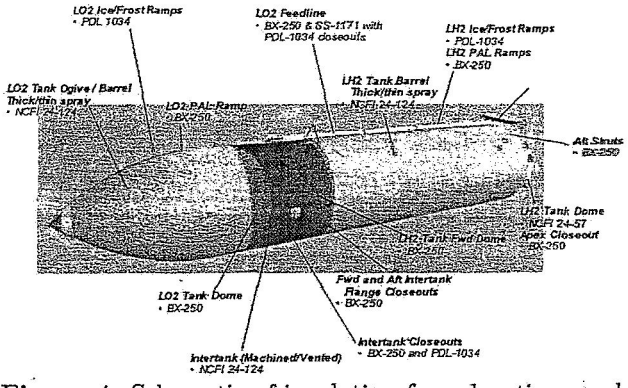

Figure 4: Schematic of insulating foam locations and types for the shuttle external tank used for STS-107. Adapted from [1], Fig. 3.2-4.

a sample of results from the debris transport analysis.

3.1 Foam Debris Shapes

The dynamic behavior of any debris piece, and by extension the aerodynamic modeling of any debris piece, is dependent upon the shape of the debris. Figure 5a has photographs of foam divots which were forced from sheets of 1"-thick foam which covers the ogive section of the ET (often called acreage foam) during experimental tests. These pieces are roughly conical (a truncated cone, or frustum), and can vary in diameter, thickness, and conical bevel angle. Figure 5b contains similar photographs of two foam divots which were ejected due to trapped air from the 3"-thick ET inter-tank flange foam which separates the region between the liquid hydrogen (LH_2) and liquid oxygen (LOX) tanks (cf. Fig. 4). These shapes are larger, and more irregular than the acreage divots, due to the greater depth of foam in these locations. The average material density for the insulating foam debris in Fig. 5 is 2.174 $\mathrm{lbm/ft^3}$.

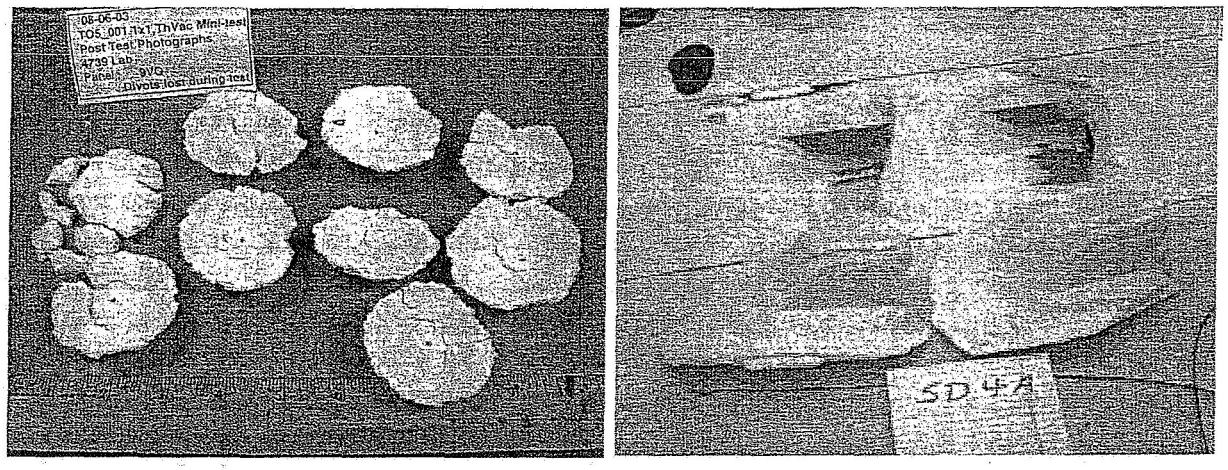

(a) Divots from ET ogive acreage foam. (b) Divots from ET flange foam.

Figure 5: Divots "popped-off" from ET foam slabs during experimental testing.

Obviously, tailoring a model to each of the individual shapes which can potentially be liberated from the ET foam is not practical. Instead we seek a model which captures the behavior of a range of shapes (and sizes). A representative idealized family of shapes is chosen to develop the model. A conical frustum geometry with beveled sides in the range $30° - 45°$ is chosen to represent the basic foam debris shapes (cf. Fig. 6). The thickness of the frustum is constrained by the thickness of the applied foam on the ET, which varies with location on the ET. These shapes are consistent with the available test samples and flight photographic data without oversimplifying the geometry. The frustum represents a family of shapes, including variations in bevel angle (θ), ratio of large diameter to thickness (D/t), and size. Actual (digitized) debris pieces are tested against the resulting models where appropriate to ensure the accuracy.

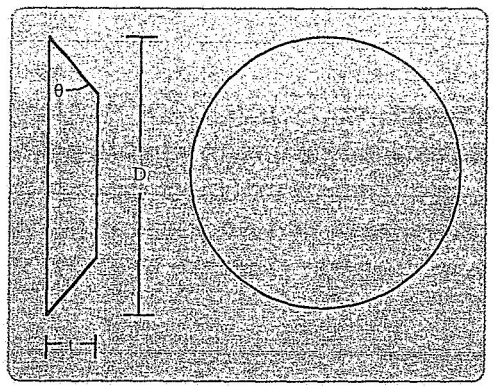

Figure 6: Conical frustum geometry representative of foam debris. Bevel angles between 30° - 45° are consistent with the test data. The thickness is constrained by the thickness of the ET foam.

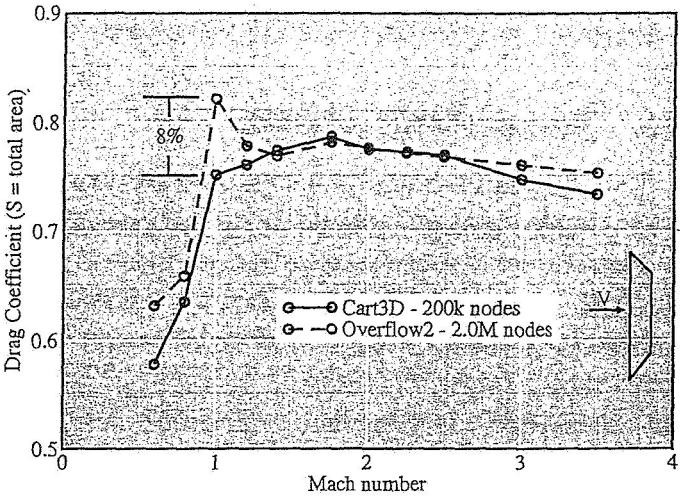

Figure 7: Drag coefficient variation for a conical acreage divot in a static, bluff-body orientation through the shuttle ascent Mach number range ($D/t = 6$, $\theta = 32°$).

3.2 Static Viscous Comparison

The Cartesian moving-body solver currently uses an inviscid approximation. The appropriateness of this approximation is examined by comparing static, bluff-body simulations of an idealized conical acreage foam piece obtained with the inviscid Cartesian package, and NASA's viscous OVERFLOW solver. A static bluff-body orientation is chosen for the comparison as the dynamic trajectories demonstrate a strong tendency to oscillate near the bluff-body, statically-stable orientation, as described in Sec. 2.2 for an unconstrained cube. The predicted drag coefficient for the relevant Mach number range seen during ascent is presented in Fig. 7. The agreement between the two solvers is very close, with the maximum variation of 8% occurring at Mach 1.0. The viscous drag increment is essentially zero ($< 0.1\%$) for these calculations. In this bluff-body orientation, the only faces which can effect the viscous drag are the beveled sides, which are located in the aft separated flow region. These aft faces experience reversed and separated regions, which when time-averaged, provide essentially no viscous stress contribution. While the viscous increment itself is negligible, the differences between the calculations at the lower Mach numbers are due to viscous effects. The viscous flow has stronger shear layers, which form stronger vortices, and also has a much wider energy band (contains energy at a wider range of frequencies) than the inviscid calculations which tend to have energy only at the shedding frequency. The stronger aft vortices induce an unsteady flow at a slightly higher Mach number in the viscous calculations (Mach 1.4 vs. Mach 1.2). Above these Mach numbers the flowfield remains steady. At the lower Mach numbers (0.6 and 0.8), these stronger vortices induce a stronger reversed flow. This stronger reversed flow creates a lower pressure on the aft face of the body, and leads to a slightly higher drag. So in general we would expect the inviscid calculations to slightly underpredict the drag through the transonic regime due to the lower strength of the separated shear layers.

Figure 7 demonstrates that an inviscid solver provides an efficient engineering approximation for these supersonic, bluff-body flows. The computational cost of computing a single 6-DOF trajectory using the Cartesian solver is nearly two orders of magnitude lower than the same trajectory computed with OVERFLOW, due to the stiffness and mesh requirements of the viscous solver. This efficiency allows a range of debris sources and release conditions to be examined computationally, so that broad behavioral trends can be discerned, rather than examining only a handful of datapoints.

3.3 Dynamic Validation

As mentioned in Sec. 2.2, there is a lack of relevant experimental data for validating numerical predictions of debris dynamics. Given the critical importance of analyzing foam debris for the RTF initiative, a test was prepared to obtain validation data for frustum foam shapes at relevant ascent conditions. This free-flight test recently took place in the NASA Ames Gun Development Facility (GDF), and will be documented in a future publication[10].

A frustum with a 1.4 inch diameter, $D/t = 5$, and a 40° bevel, was fabricated from High-Density Polyethylene (HDPE). This material was chosen to match the density ratio between foam at flight conditions and the test article in the sea-level test chamber. The frustum model was fired with the small diameter initially oriented into the wind. Translation and rotation data were obtained over 12 feet of trajectory from high-speed cameras. In addition, the response of the debris to a perturbation could be obtained by "tripping" the debris projectile before it entered the test section. This perturbation both changes the orientation of the model as it enters the test chamber and provides a high initial rotation rate. Comparisons of the measured axial translation distance, and the model pitch and yaw variation, against simulated trajectories using the Cartesian moving-body solver are presented in Figs. 8 and 9. The comparison in Fig. 8 is for an untripped trajectory at an initial Mach number of 2.74. The agreement between the computed data and the experiment is excellent. Both the computation and measured data demonstrate that the foam frustum has a low-amplitude (±10°) damped oscillation about the bluff-body, static-stability orientation. Figure 9 presents the response to a perturbation for an initial Mach number of 2.56. Again the agreement between the simulation results and the measured data is excellent for both translation and rotational orientation. The perturbation response shows a larger amplitude (±45°) damped oscillation about the bluff-body orientation.

There are a combination of factors which contribute to the observed dynamic stability of the foam frustum shapes. For the same physical reasoning as the cube shape (Sec. 2.2), the bow shock provides a restoring moment for low-amplitude oscillations. Further, for a frustum with the smaller diameter moving into the wind, the edge-on orientation also provides a strong restoring moment due to the wedge shock which forms over the leading edge in large-amplitude oscillations. Since the material density of the foam is extremely low, the frustum models have very little rotational inertia in order to overcome this deep stability "well". The aerodynamic and inertial asymmetry of actual divots (cf. Fig. 5) can offset this stability, and this effect must be taken into account when developing a model using idealizing geometries.

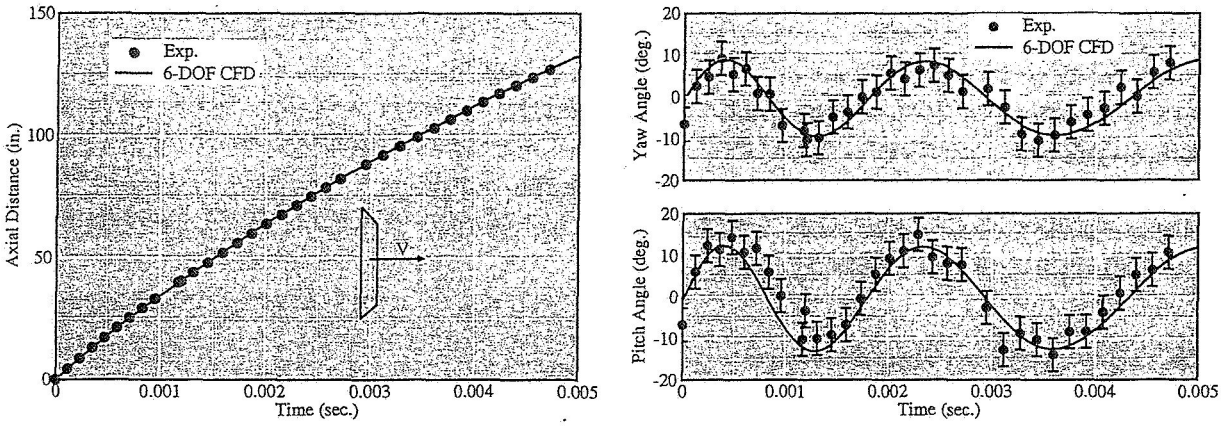

(a) Axial displacement. (b) Pitch and yaw orientation.

Figure 8: Comparison of free-flight and computed translation and rotation variations for untripped frustum trajectory obtained in the NASA Ames GDF[10]. Initial Mach number is 2.74. Uncertainty approximated from visual inspection of reduced data. ($D/t = 5$, $\theta = 40°$).

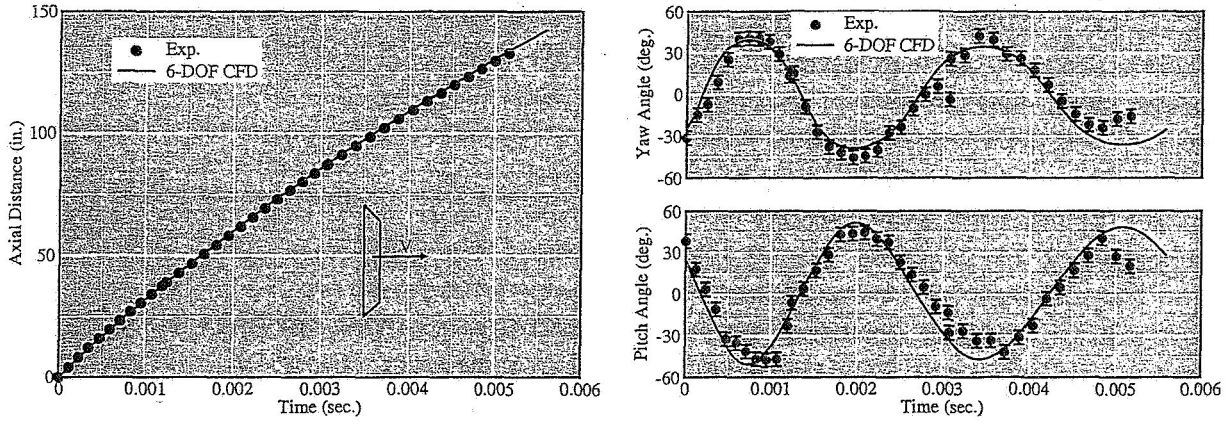

(a) Axial displacement. (b) Pitch and yaw orientation.

Figure 9: Comparison of free-flight and computed translation and rotation variations for initially perturbed frustum trajectory obtained in the NASA Ames GDF[10]. Initial Mach number is 2.56. Uncertainty approximated from visual inspection of reduced data. ($D/t = 5$, $\theta = 40°$).

3.4 Drag Modeling

Figure 5 shows photographs of foam divots which were either forced from foam sheets, or ejected due to voids containing trapped air. Experimental evidence indicates that a range of shapes, typically thin and roughly conical, can potentially be shed from the ET acreage foam. Computational efforts to characterize the foam aerodynamics thus concentrate on idealized frustum shapes of various dimensions. The difference between a modeled axisymmetric frustum shape and the experimental evidence of Fig. 5 highlights the difficulty involved in modeling the debris aerodynamics for use in a ballistic code. A debris piece whose shape and size is only generally known is hypothetically shed from a particular location. The velocity

and angular rotation of this shedding event are unknown, and in fact the debris may linger in the boundary layer until popping into a high-speed stream. Trajectory calculations are inherently sensitive initial-value problems, yet in our modeling we cannot accurately state any of the initial conditions! Predicting any single trajectory is thus an impossibility, and the approach here is to predict an average trajectory. With this nominal trajectory in-hand, variations (for lift, drag, etc.) can then be superimposed.

In order to develop a model of the dynamic behavior of uncontrolled debris pieces, a range of 6-DOF trajectories must be computed with the debris released in different orientations and with different initial rotation rates. The initial orientations are biased towards the edge-on configuration, as this is the orientation the pieces shed from the ET. Similarly, the initial rotation rates must also be consistent with the debris pop-off mechanism. Currently, there is no available data for the initial rotation rate of debris shedding. Physical arguments can be used to limit the likely initial rotation rate to less than 25-50 Hz for conical frustums with sizes up to $D = 6$ inches. Hence, the simulations presented in this work vary the initial rotation rate for either of the "pitch" axes up to a magnitude of 20 Hz (cf. Fig. 10). Similarly, a significant initial rotation rate about the major axis of the debris is unlikely. However, this major-axis rotation rate, and the rates about the other two axes, are never explicitly set to zero. A small initial value is always provided so that any potential coupling between the axes due to small perturbations can develop.

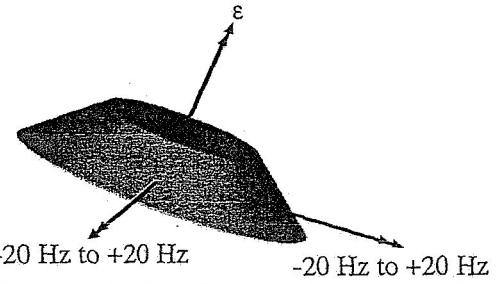

Figure 10: Distribution of initial rotation rates for foam debris shapes. These conditions should be consistent with the physical pop-off mechanism for debris shedding from the ET. The initial rotation rate is varied up to a magnitude of 20 Hz about either of the pitch axes.

Before a model for a range of shapes is developed, the typical dynamic behavior of a single representative foam frustum shape is presented. A set of simulations for the frustum presented in Fig. 7 using static, forced-tumble, and unconstrained 6-DOF trajectories released at $M_\infty = 2.5$ are shown in Fig. 11. The behavior of the unconstrained 6-DOF trajectories is similar to the results for the cube (Sec. 2.2) and the GDF validation (Sec. 3.3): in the supersonic Mach number range the debris oscillates about the bluff-body orientation, and exhibits a tumbling behavior after passing through the transonic regime. The static simulations with the frustum held fixed with the maximum and minimum frontal area exposed provide bounds on the 6-DOF behavior.

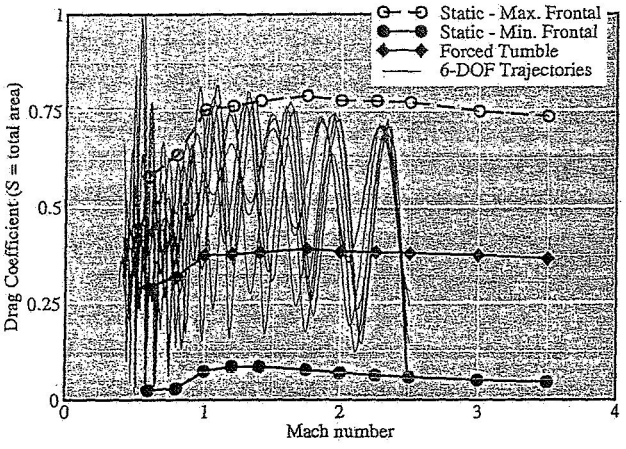

Figure 11: Drag variation for static, forced-tumble, and sample 6-DOF trajectories for a typical frustum shape ($D/t = 6$, $\theta = 32°$).

While the range of possible dynamic behavior exhibited by even a single foam frustum

piece is complex, an important observation from Fig. 11 is that the ensemble average of the 6-DOF trajectories is bounded by the static data. This echoes the results for the unconstrained cube shape in Fig. 3. This ability to bound the data is an important feature of the drag modeling, and allows the modeling methods to generalize to the different shapes encountered with other debris sources.

While we can bound the behavior of a single frustum foam piece, we still require a method of characterizing the behavior over a range of foam pieces. To account for this variation we use an ensemble average of the static and forced-tumble bounding curves over a range of frustum pieces ($D = 1.8 - 12$ in., $t = 0.5 - 3$ in., and $\theta = 32° - 45°$). Further, we need a method of defining the drag coefficient from these disparately-sized pieces that can collapse a range of data to a single curve. The use of the frustum total area provides this desired scaling. The total area is unambiguous, in contrast to a measure such as frontal area, so that irregular pieces such as Fig. 5b can be accommodated. Since the frustum pieces are beveled, the sides are always contributing to drag, as opposed to a piece such as a cylinder, where an axial elongation can change the total area without appreciably changing the drag. This convenience of geometry allows the computed results for the static maximum frontal area and forced-tumble simulations over the range of frustum pieces examined to collapse to a within ±10% in drag coefficient variation relative to the average. The drag variation with Mach number for all of the simulated frustum pieces is presented in Fig. 12, along with the ensemble average and a 10% variation. The static minimum frontal area calculations also collapse well, though the variation is slightly greater than 10% of the average value. This variation will not adversely effect the model development to follow.

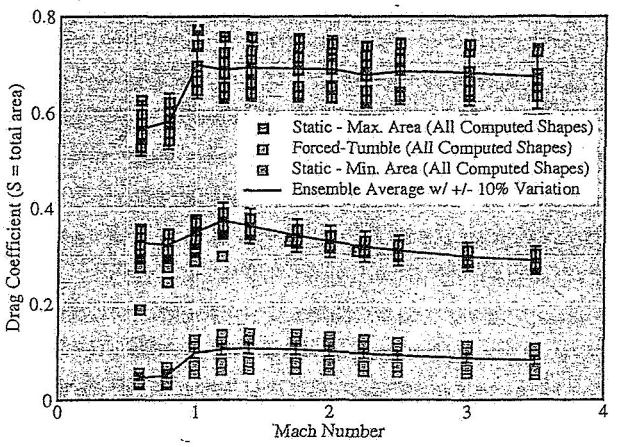

Figure 12: Computed drag coefficient variation over a range of shapes for static and forced-tumble results, along with an ensemble-average.

Figure 13 represents a summary of the discussion so far. A set of unconstrained 6-DOF trajectories for a range of shapes, including ideal frustums and digitized actual shapes, are shown along with the ensemble-average curves from Fig. 12. All of the 6-DOF trajectories are roughly bounded by the static ensemble-average curves, including the trajectories of actual asymmetric debris shapes. The 6-DOF trajectories cover a range of behavior, with the drag coefficient varying by an order of magnitude within a given trajectory. We require a method of determining the nominal behavior over this range of trajectories. The temptation is to use some type of averaging procedure over the 6-DOF trajectories. For example, time-averaging the drag coefficient to determine a nominal drag coefficient for each trajectory. Unfortunately, these methods do not provide accurate results due to the non-linearity of the behavior. As an example, a trajectory may have a large drag value for only a

short time period early in the trajectory, and low values the remainder of the time, yet still have a relatively large velocity throughout the trajectory. This is due to the non-linearity of the problem and the dramatic drop in dynamic pressure during the trajectory.

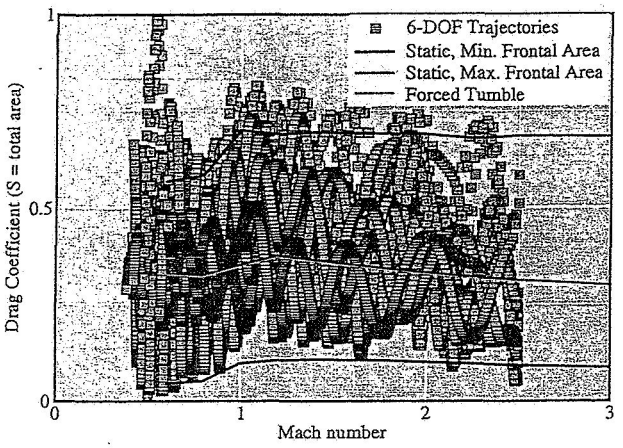

Figure 13: Comparison of drag coefficient variation for unconstrained 6-DOF trajectories with ensemble-average over a range of shapes of static and forced-tumble computed results.

Rather than use an averaging procedure, the nominal behavior is determined from the bounds of the 6-DOF trajectories. Drag coefficient variation with Mach number does not provide this bounding however, as just discussed. For the debris transport problem, kinetic energy variation with distance provides a relevant measure of the model fitness. Kinetic energy at impact correlates with the damage potential, and the distance between debris shedding and impact is more relevant than the travel time since the debris analysis takes place in the moving, shuttle-fixed coordinate frame. A non-dimensional kinetic energy,

$$\frac{1}{2}\frac{m}{\rho_\infty L^3}\left(\frac{V}{a_\infty}\right)^2 \tag{1}$$

where m is the mass, V the velocity, a_∞ the freestream sonic speed, and L is a length-scale of the debris. The length-scale is chosen as the cube root of the debris volume. This non-dimensionalization scales the results of all the computed 6-DOF debris trajectories into a single plot in Fig. 14. The results of integrating trajectories through a uniform stream using the drag coefficient variation with Mach number for the static and forced-tumble ensemble-average curves are also included. The static minimum frontal areas curves are not presented for clarity. A range of behavior is possible for the static and forced-tumble integrated trajectories depending upon the surface-volume ratio chosen (drag scales with surface area, while mass scales with the volume). In Fig. 14, the surface-volume ratio is varied through the sizes of debris which can shed from the ET. This range of surface-volume ratios provides a band of behavior. Surprisingly (after seeing Fig. 13), the forced-tumble results provide a good estimate of the lower bound for the kinetic energy variation. The upper bound is obtained by using the static, maximum frontal area ensemble average curve. Note that the 6-DOF trajectories in Fig. 14 include a range of both ideal frustum pieces and actual digitized divots. With these two bounds the nominal behavior can be easily determined by simply averaging the upper and lower bounds (Fig. 15).

The forced-tumble, static, and nominal bands in Figs. 14 and 15 are the drag models. By appropriately choosing the surface-volume ratio these models can provide a lower bound, upper bound, or nominal value respectively for the impact kinetic energy for any acreage foam debris shedding event. Since the lower and upper bounds on the drag variation are

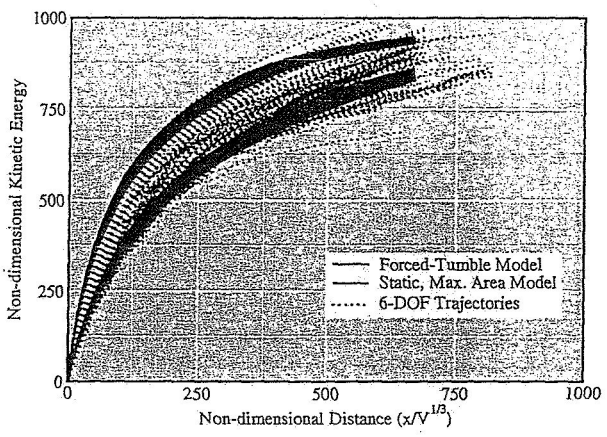

Figure 14: Comparison of kinetic energy variation for unconstrained 6-DOF trajectories and integrated trajectories using the ensemble-average curves from Fig. 13 for a range of shapes. Trajectories released at Mach 2.5.

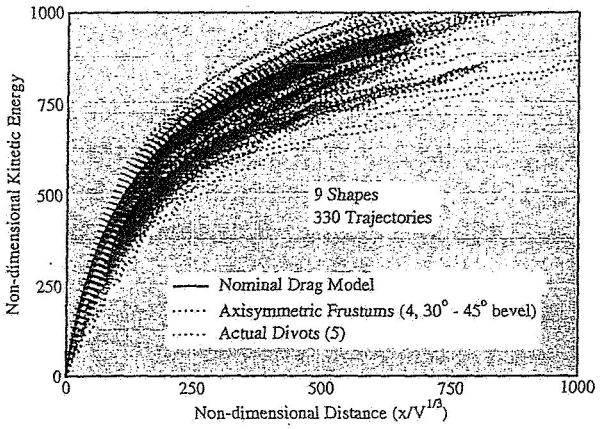

Figure 15: Comparison of kinetic energy variation for unconstrained 6-DOF trajectories and integrated trajectories using a nominal drag model based on the ensemble-average curves for a range of shapes. Trajectories released at Mach 2.5.

known, a statistical analysis can also be undertaken by providing a probability distribution between the bounds.

Similar to the validation of the Cartesian methods used to develop these models, the NASA Ames GDF test data is used to validate the resulting models themselves. Three data sets are chosen: a low- (±10°), medium- (±45°), and high-oscillation (±90°) trajectory representing a high-, medium-, and low-drag case respectively. The variation of axial distance with time for these three trajectories is compared against predictions using the debris drag models in Fig. 16. In these plots the greater the distance traveled at a given time the lower the average drag during the trajectory. Using the appropriate surface-volume ratio from the test article, the models predict the axial displacement (a measure of the drag force) for the low, nominal, and high drag orientations extremely well.

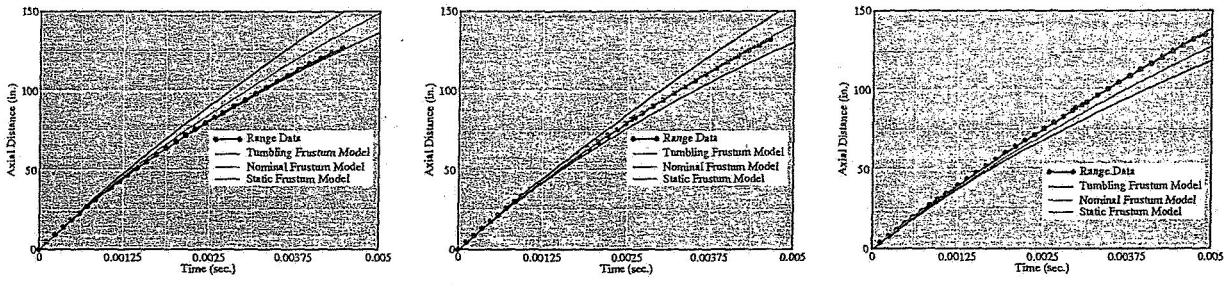

(a) Low-oscillation (±10°), high-drag trajectory ($M_\infty = 2.71$).

(b) Med-oscillation (±45°), med-drag trajectory ($M_\infty = 2.56$).

(c) High-oscillation (±90°), low-drag trajectory ($M_\infty = 3.00$).

Figure 16: Validation of the drag models presented in Figs. 14 and 15 against the free-flight range data from the NASA Ames GDF[10].

3.5 Crossrange Model

The previous section outlines validated drag models for foam debris shedding from the space shuttle ET during ascent. The models are used in the debris transport ballistic code to predict potential debris impact velocities, however some method of accounting for the lift generated by each piece must be included. The results in Figs. 14 and 15 demonstrate that the average drag for the oscillating trajectory of an idealized frustum and the tumbling trajectory of a highly asymmetric debris piece are similar. This is not the case when considering the crossrange behavior. The dynamically-stable oscillating frustum generates virtually no crossrange, as the lift force oscillates first in one direction then the other to little net effect. Fig. 17 shows a time-sequence of the orientation and computed pressure on an actual foam divot which is asymmetric both aerodynamically and inertially. This trajectory develops significant crossrange as the debris rotates about all three body axes.

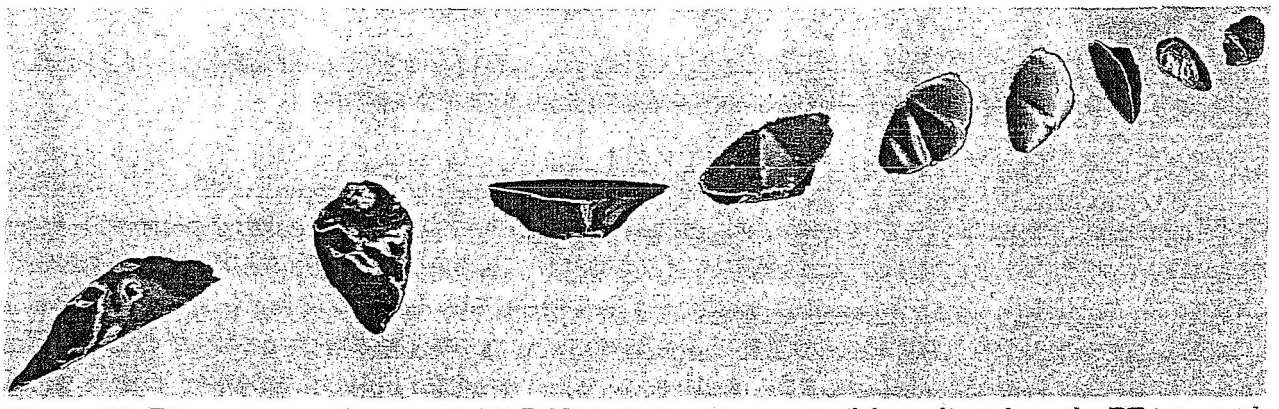

Figure 17: Time sequence of a computed 6-DOF trajectory for an actual foam divot from the ET inter-tank flange region. Debris colored by surface pressure. A subset of the computed timesteps is shown for clarity.

The lift force vector for an arbitrary piece of debris can potentially act in any direction, and hence is referred to here as a crossrange force. The amount of lift a piece can sustain is partly a function of its relative inertia: the larger the relative inertia the longer the debris can sustain a lifting orientation. Similarly, shape and initial conditions play a major role in the lifting behavior. Simply using an approximation for the lift-drag ratio for an average piece is not appropriate. Figure 18 graphically demonstrates the approach taken here. A complete crossrange cone is superimposed on a zero-lift trajectory to determine a potential impact zone. Rather than model the aerodynamic properties, a crossrange envelope is developed from the results of the Monte Carlo process outlined in the previous section for generating debris trajectories. This crossrange envelope is superimposed on the zero-lift trajectory for each computed ballistic trajectory, in this example foam being shed from the ET flange region. The crossrange envelope determines *where* the debris can potentially impact, while the drag model determines the impact velocity. Further, a complete statistical distribution of crossrange behavior can be provided so that a probability function can be queried for any point within the envelope. The crossrange envelope is scaled by the debris length scale to represent different sizes in a single function, which naturally provides an increase in crossrange for larger pieces.

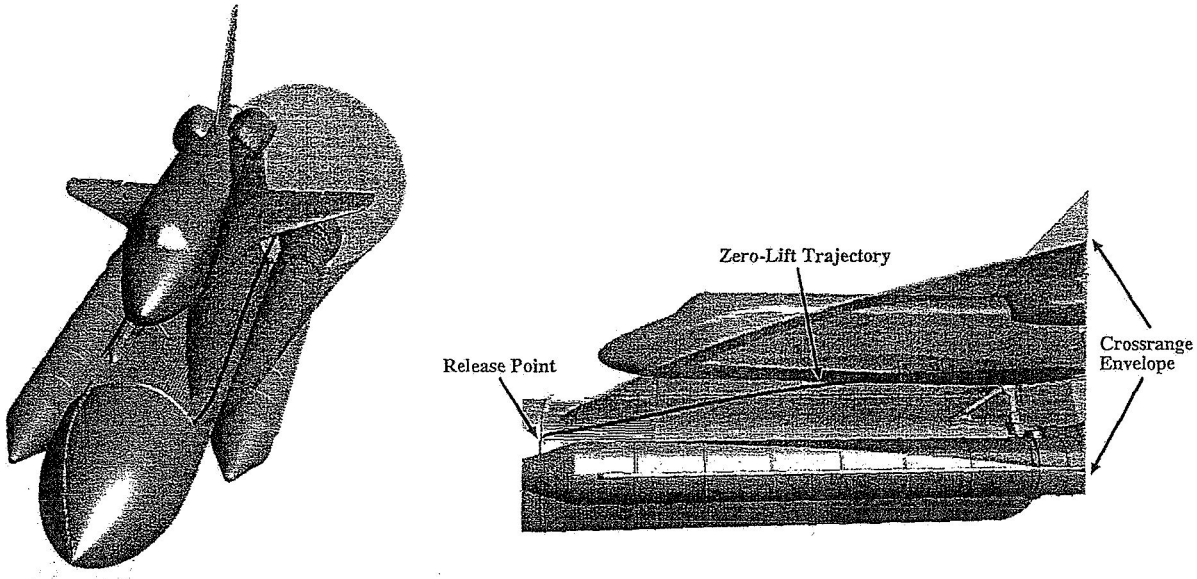

Figure 18: Crossrange envelope superimposed upon the computed ballistic zero-lift trajectory. A statistical distribution of the crossrange within the envelope can be used for a risk analysis.

Several types of shapes were used to develop the crossrange envelope in order to provide a representative distribution. These include actual digitized shapes, idealized frustums, ideal frustums with the center of mass offset, and mildly asymmetric shapes such as elliptical frustums with the small diameter slightly offset from the larger. Figure 19 presents the crossrange behavior from the 6-DOF calculations at a release Mach number of 2.5. The ideal frustums typically generate little crossrange, as discussed above, however even a small asymmetry in the geometry leads to the potential for large crossrange excursions.

The crossrange behavior in Fig. 19 is limited by curves which show a nearly constant lift, however the pieces are typically both oscillating and tumbling. This apparently diverse behavior is caused by the piece holding a high-lift orientation early in the trajectory. This orientation provides a large crossrange inertia. Since the debris pieces decelerate extremely rapidly, the dynamic pressure drops very quickly, and hence when the piece is in an opposite orientation the restoring force is much smaller. Hence the pieces appear to be constantly lifting, however they are in fact simply responding to an initial "kick" due to orientation that cannot be compensated for later in the trajectory. The crossrange behavior over a range of ascent conditions, and dynamic pressures, must be developed. Figure 20 presents a sample of trajectories computed for an actual divot shape using the same release conditions

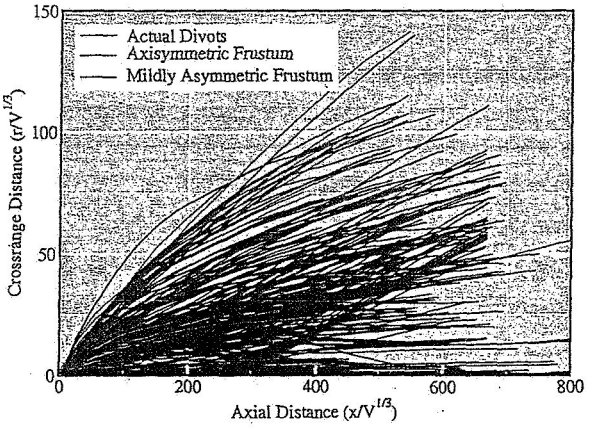

Figure 19: Computed crossrange behavior from Monte Carlo 6-DOF trajectories for foam debris shapes at a release Mach number of 2.5.

while varying the Mach number and altitude. While dynamic pressure decreases substantially in the shuttle ascent trajectory between Mach 2.5 and 3.5 due to the drop in freestream density with increasing altitude, this reduction is offset somewhat by the increase in static pressure behind the shock at the higher Mach number. Further, while the crossrange behavior at high dynamic pressure release conditions is characterized by a large crossrange kick early in the trajectory, at lower dynamic pressure conditions the behavior changes. For low-q releases the debris tends to tumble due to the low restoring moment, but since the drag force is also greatly reduced, there is little change in dynamic pressure during the trajectory. This leads to a roughly constant magnitude crossrange force that generates large crossrange excursions which are built over longer time periods, as opposed to an initial hard kick. This behavior is seen through Mach 5.0 during the ascent trajectory, after which the ET is released. The net result is that the high-q and low-q simulations tend to show similar crossrange behavior, even though they achieve the results through different mechanisms.

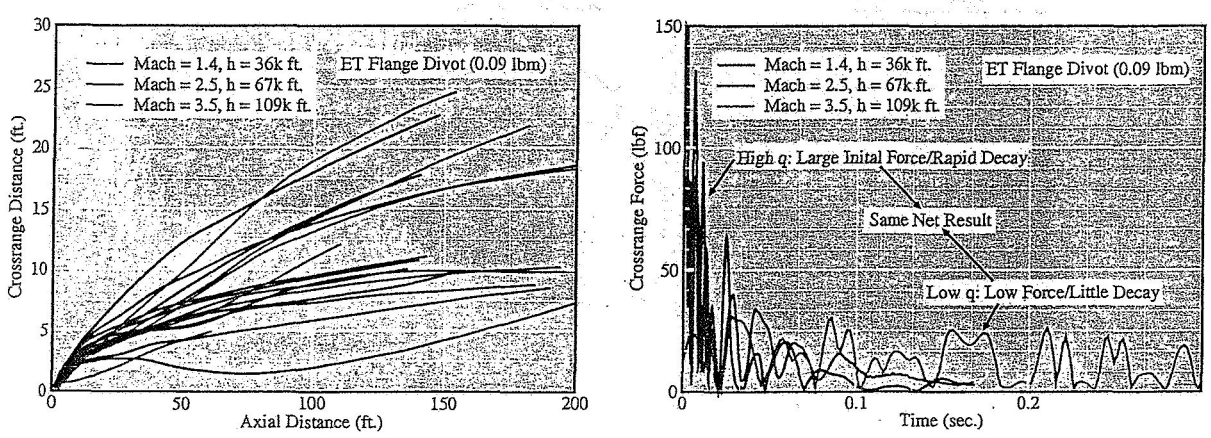

(a) Crossrange Variation (b) Crossrange Force Variation

Figure 20: Crossrange envelope superimposed upon the computed ballistic zero-lift trajectory. A statistical distribution of the crossrange within the envelope can be used for a risk analysis.

3.6 Debris Transport Example

To conclude the discussion of foam aerodynamic modeling, the results of applying the debris transport analysis ballistic code and post-processing crossrange envelope to a sample trajectory is presented. The crossrange envelopes in Fig. 18 show a zero-lift trajectory emanating from the ET flange region computed with the debris transport ballistic code using the nominal drag model from Sec. 3.4. Superimposed upon this baseline trajectory is a crossrange cone to determine the potential impact locations. The intersection of this cone with the SSLV indicates that the fuselage and wing of the orbiter have potential for debris impacts from this flange location, along with regions of the left solid rocket booster. Figure 21 presents these potential impacts on the SSLV colored by the impact kinetic energy. The farther downstream the debris travels before impact the greater the impact kinetic energy as the aerodynamic drag is constantly increasing the relative velocity between the debris and

the orbiter.

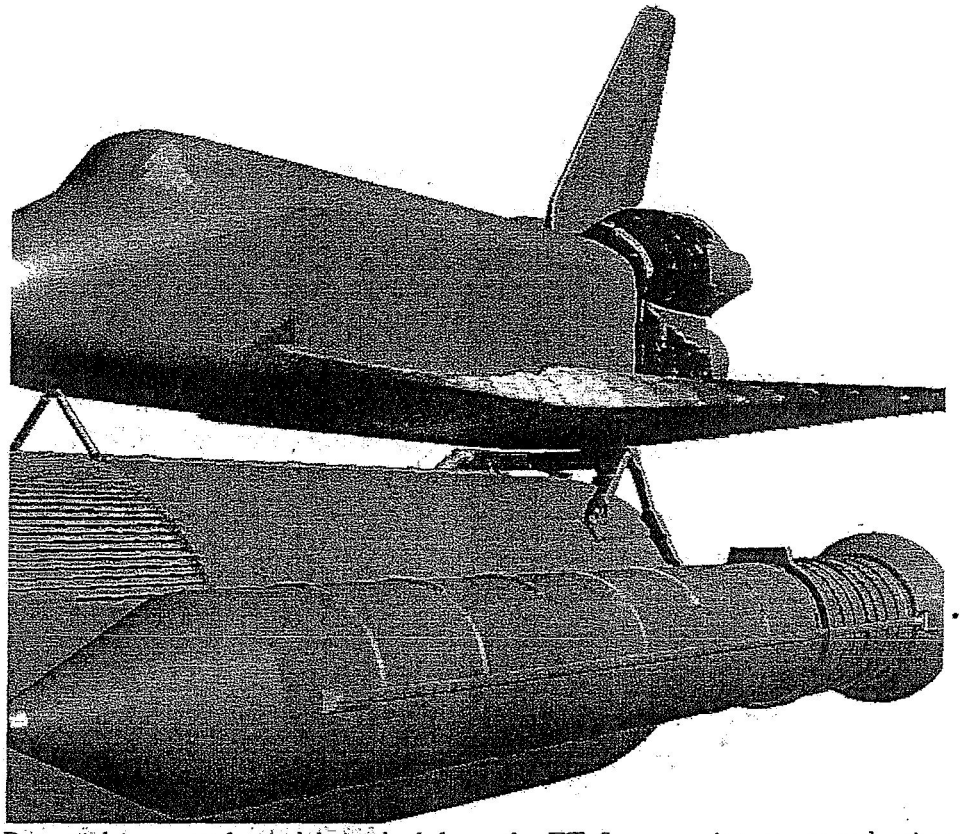

Figure 21: Potential impacts from debris shed from the ET flange region computed using the zero-lift trajectory and crossrange enveloped shown in Fig. 18. Locations colored by impact kinetic energy.

4 Summary

Determining the aerodynamic characteristics of unconstrained debris pieces requires unconventional modeling techniques, as traditional methods developed for maneuvering aircraft are inappropriate. Automated Cartesian CFD methods provide a valuable tool for this analysis using a combination of static, prescribed-motion, and fully-coupled 6-DOF simulations. The use of CFD methods provides an efficient, rapid-response tool which can easily accommodate arbitrary geometric shapes. A process for modeling the behavior of the types of debris encountered during ascent of the SSLV has been described. This process focuses on modeling the resulting behavior of Monte Carlo 6-DOF simulations, rather than developing proximate aerodynamic models. The latter is a longer-term research topic which can be leveraged from the current engineering analysis.

An analysis of insulating foam debris shed from the acreage regions of the shuttle external tank provided a detailed discussion of the approach. The CFD methods used in developing aerodynamic models for foam debris were validated against free-flight, ballistic-range data matching relevant ascent conditions. Drag and crossrange models for use in separate pre-

existing debris transport analysis tools were developed to cover the range of foam debris shapes known to possibly shed from the external tank. The drag models were also validated against ballistic-range data. Finally, an example debris transport analysis of the potential impact of ET flange foam using the developed models was presented.

The emphasis of this work is the development of an efficient process for modeling debris using CFD methods. This process has been applied to various debris sources beyond ET insulating foam, including the ET LOX frost ramps, insulating cork on the solid-rocket boosters, frost and ice on the ET acreage regions, and ice which can form on the ET feedline brackets. The flexibility of the Cartesian methods, and the generality of the modeling approach, allows the dynamic behavior of these diverse debris sources to be analyzed in a systematic manner.

Acknowledgments

The authors gratefully acknowledge the NASA Ames GDF test team, especially Jeff Brown, Dave Bagdanoff, Leslie Yates, and Michael Wilder, for the use of the foam ballistic range data. William Chan of NASA Ames Research Center graciously provided the viscous frustum simulations in Sec. 3.2. We would also like to thank Ray Gomez and Phil Stuart of Johnson Space Center for their support and advice during this project. Scott Murman was supported by NASA Ames Research Center (contract NAS2-00062) during this work.

References

[1] Columbia Accident Investigation Board Report, Vol. 1, Aug. 2003.

[2] Gomez, R.J., Vicker, D., Rogers, S.E., Aftosmis, M.J., Meakin, R.M., Chan, W.M., and Murman, S.M., "STS-107 Investigation Ascent CFD Support," AIAA Paper 2004-2226, July 2004.

[3] Murman, S.M., Aftosmis, M.J., and Berger, M.J., "Implicit Approaches for Moving Boundaries in a 3-D Cartesian Method," AIAA Paper 2003-1119, Jan. 2003.

[4] Murman, S.M., Aftosmis, M.J., and Berger, M.J., "Simulations of 6-DOF Motion with a Cartesian Method," AIAA Paper 2003-1246, Jan. 2003.

[5] Jespersen, D.C., Pulliam, T.H., and Buning, P.G., "Recent Enhancements to OVERFLOW," AIAA Paper 97-0644, Jan. 1997.

[6] Murman, S.M., Chan, W.M., Aftosmis, M.J., and Meakin, R.L., "An Interface for Specifying Rigid-Body Motion for CFD Applications," AIAA Paper 2003-1237, Jan. 2003.

[7] Hansche, G.E. and Rinehart, J.S., "Air Drag on Cubes at Mach Numbers 0.5 to 3.5," *Journal of the Aeronautical Sciences*, 19:83–84, 1952. Also *Fluid-Dynamic Drag*, Hoerner, S.F., 1965. pg. 16–14.

[8] Murman, S.M. and Aftosmis, M.J., "Cartesian-Grid Simulations of a Canard-Controlled Missile with a Spinning Tail," AIAA Paper 2003-3670, Aug. 2003.

[9] Murman, S.M., Aftosmis, M.J., and Berger, M.J., "Numerical Simulation of Rolling-Airframes Using a Multi-Level Cartesian Method," *Journal of Spacecraft and Rockets*, 41(3):426–435, 2004. Also AIAA Paper 2002-2798.

[10] Brown, J., Bogdanoff, D., Yates, L., and Wilder, M. private communication, Dec. 2004.